Commun Nonlinear Sci Numer Simulat 46 (2017) 135–152

Contents lists available at ScienceDirect

Commun Nonlinear Sci Numer Simulat

journal homepage: www.elsevier.com/locate/cnsns

Research paper

A biophysical model of tumor invasion

Sashikumaar Ganesan[a,*], Shangerganesh Lingeshwaran[b]

[a] Department of Computational and Data Sciences, Indian Institute of Science, Bangalore, 560 012, India
[b] Department of Humanities and Sciences, National Institute of Technology, Goa, 403 401, India

ARTICLE INFO

Article history:
Received 8 April 2016
Revised 28 September 2016
Accepted 18 October 2016
Available online 19 October 2016

Keywords:
Cancer invasion
Nonlinear diffusion
Nonlinear haptotaxis effect
Finite element simulations
Breast geometry

ABSTRACT

Three-dimensional finite element computations of a cancer invasion model with nonlinear density-dependent diffusion and haptotactic sensitivity function are presented. The nonlinear model includes three key variables, namely the cancer cell density, the extra cellular matrix (ECM) density and the matrix degrading enzymes (MDE) concentration. In order to investigate the effects of tumor growth and invasion on a realistic geometry, the interactions between the cancer cells and the host tissue are incorporated into the model. The convergence study and the validation are first performed for the proposed numerical scheme. Then the effects of nonlinear diffusion and ECM-dependent haptotaxis on tumor growth and invasion in three-dimensional geometries are presented. Finally, several numerical simulations are performed with different combinations of nonlinear diffusion and haptotaxis functions to get an insight into the tumor invasion on a realistic (breast) geometry. The proposed computational model can be used to predict the location and shape of the tumor in realistic geometries at a particular instance.

1. Introduction

The incidence of cancer among the people around the world has grown rapidly over the last decade. Globally, cancer is becoming the second leading cause of death after cardiovascular diseases [1]. Especially, the incidence of breast cancer is increased among women [22]. Metastasis (the process of spreading and formation of secondary tumours) behavior of cancer cells is the major cause of death in cancer patients. Therefore, prediction of tumor stage, size and progression is very crucial for cancer treatments, in addition to an early detection of the tumor.

Mathematical model is one of the useful and inexpensive approaches to determine and predict the stage, size and progression of tumors in realistic geometries. Moreover, these models can be used to get an insight into the cancer growth and invasion. Further, they can also be used to analyze the tumor size and shape for cancer treatment and surgical plannings. Several mathematical models have been proposed in the literature over the last few decades to model the cancer dynamics, see for example, [4,16,26,32,42]. The invasion of cancer cells is modeled either by using a discrete cell-based approach that focus on individual cell behaviors [3] or by using a continuum approach [2,17] that deals with the evolution of the cancer cell densities. Under the assumption that the initial number of tumor cells are relatively small, one can get computationally reasonable results using the discrete cancer invasion model. However, the above assumption is too strong to identify clinically significant size of tumor with the current imaging techniques such as MRI, CT-Scan etc. Therefore, we consider the continuum tumor invasion mathematical model in this study.

* Corresponding author.
E-mail addresses: sashi@cds.iisc.ac.in (S. Ganesan), shangerganesh@nitgoa.ac.in (S. Lingeshwaran).

http://dx.doi.org/10.1016/j.cnsns.2016.10.013
1007-5704/

A number of numerical methods have been proposed in the literature for computations of cancer invasion and related continuum mathematical models. The finite difference method [9,10], finite volume method [24], method of lines [19] are the most commonly used methods in the literature for cancer migration models. Apart from the numerical studies, mathematical analysis such as existence of the solutions, boundedness and exponential convergence of the solutions have also been reported in the recent studies, see for example [23,40,41] and the references there in. In general, finite element method (FEM) is preferred for computations on complex geometries, especially, computations on realistic geometries such as brain, breast, prostate etc. Zheng et al. [45] and Peterson et al. [31] proposed an adaptive finite element method in two-dimensional (2D) domain for vascularized tumor models to simulate the angiogenesis process. Further, discontinuous Galerkin finite element methods have also been successfully applied in [15] for haptotaxis-chemotaxis problems in 2D domains. To study the tumor growth based on the continuum theory of mixtures, a 2D mixed finite element method has been proposed in [12]. Recently, Vilanova et al. [43] have performed numerical simulations for discrete/continuum tumor angiogenesis model using finite element method with growth of capillaries in 2D spatial domain. An implicit level set finite element numerical scheme for reaction-diffusion-advection equations related to tumor invasion models on an evolving in-time-hypersurface on two-dimensional domain has been proposed and studied in [35]. A positivity preserving finite element method has also been proposed and studied in [37,38] for chemotaxis type problem (not for cancer invasion models) on both two- and three-dimensional spatial domains. Most of these studies have also been carried out for cancer or related models in two-dimensional domains. Nevertheless, only a few numerical studies on cancer invasion have been reported for realistic geometries. Moreover, the work of Gavaghan et al. [20] shows the necessity of numerical computations for realistic biological domain in cancer invasion studies for clinicians. Clatz et. al [11] proposed a reaction-diffusion three-dimensional model to study the growth of glioblastomas multiforma (GBM) tumors and accomplished computations for invasion of GBM tumors using FEM on realistic brain spatial domain. However, the authors considered only the tumor density in their model. Apart from this work, the authors are not aware of any numerical computations using FEM on realistic geometries to study the cancer invasion.

In this work, we consider a highly nonlinear coupled cancer invasion 3D model with density-dependent diffusion and haptotaxis functions. Further, the finite element scheme for solving a tumor model on realistic 3D domain is proposed in this work. The considered mathematical model focuses on the spatial competition between cancer cells and host tissues. In addition, the considered model is capable of explaining the invasion of avascular tumors and metastasis behaviors of the cancer cells in a detailed manner. The proposed finite element scheme is also implemented for the model with various density-dependent nonlinear diffusion and haptotactic sensitivity functions.

The paper is organized as follows. In Section 2, the governing equations of cancer invasion model consists of cancer density equation, ECM density equation and MDE concentration equation are introduced. Then the dimensionless form of the model equations and the initial and boundary conditions of the cancer invasion model are also presented in that section. Further, different density-dependent nonlinear diffusion and haptotactic sensitive functions are provided in Section 2 for the proposed cancer invasion model. Variational formulation of the cancer model, the finite element discretization, and the solution procedure for the nonlinear system are presented in Section 3. The convergence study, grid independence test and validation of the proposed numerical scheme are presented in Section 4. Effects of various nonlinear diffusion functions and haptotactic functions on both cube and realistic geometries are also presented in Section 4 and 5 respectively. Finally, the observations of this study are summarized in Section 5.

2. Tumor invasion computational model

In this section, a three-dimensional cancer invasion model is presented. The unknown functions in the model are the cancer cell density u, the extra cellular matrix (ECM) density v and the matrix degrading enzymes (MDE) concentration w. Let $\Omega \subset \mathbb{R}^3$ be the computational domain and $\partial\Omega$ be the boundary of the domain. The computation starts with the initial time zero and it ends at a specified time I. Here, we briefly recall the derivation of cancer invasion model presented in [2] with some modifications. Further, this model simulates micro-environmental interactions of cancer cells aiming to anticipate its spatio-temporal evolution in realistic geometries.

2.1. Mathematical model

The migration of the cancer cells into the ECM domain as well as the proliferation of cancer cells are described by a set of partial differential equations (PDEs). The density of cancer cells in Ω which has non-uniform growth and invasion in the time interval $(0, I)$ is modelled by the reaction-diffusion equation

$$\frac{\partial u}{\partial t} = \nabla \cdot J(u, v, w) + S(u, v) - T(u) \qquad \text{in } \Omega \times (0, I). \tag{2.1}$$

Here, J represents the motility flux of the cancer cells, S the proliferation rate of the cancer cells and T the death rate or anti cancer treatment effects of tumor. The motility flux of tumor cells can be expressed as a linear combination of two different fluxes,

$$J = J_{diffusion} + J_{haptotaxis},$$

where $J_{diffusion}$ is random motion of tumor cells and $J_{haptotaxis}$ is a diffusion due to the effect of haptotaxis, that is, a directed movement of cells towards the gradient of fixed or bounded components such as non-diffusional ECM. In general diffusion flux and the haptotactic flux are modelled by

$$J_{diffusion} = -D_u(u, v, w)\nabla u, \qquad J_{haptotaxis} = \chi_0(v)u\nabla v,$$

where the diffusion coefficient $D_u(u, v, w)$ is a constant or a function of the cancer cell density, ECM and MDE, and $\chi_0(v)$ is the haptotactic sensitivity function. In addition to the random and haptotaxis diffusion, cancer cells can proliferate in an uncontrolled manner without obeying the usual signal of the healthy cells. In general, the proliferation rate can either be a simple linear function or a logistic growth or based on the Gompertz law, and the respective models are given by

$$S(u, v) = \mu\left(\frac{u}{U} - \frac{v}{V}\right), \quad S(u, v) = \mu u\left(1 - \frac{u}{U} - \frac{v}{V}\right), \quad S(u) = \mu u \ln\frac{K}{u}.$$

Here, $\mu > 0$ is a growth rate constant, K is the carrying capacity of cells and U, V are the reference densities of u and v, see for example, [10,27,30]. Further, assume that the death rate of cancer cells $T(u)$ is zero and use the logistic growth rate model. Hence, the governing equation for the tumor cell density become

$$\frac{\partial u}{\partial t} = \nabla\cdot(D_u(u, v, w)\nabla u) - \nabla\cdot(\chi_0(v)u\nabla v) + \mu u\left(1 - \frac{u}{U} - \frac{v}{V}\right) \qquad \text{in } \Omega\times(0, I). \tag{2.2}$$

We next consider the continuum model for ECM. In tumour growth, MDEs, for example, matrix metalloproteinases, produced by the cancer cells degrade most of the components of ECM. It also degrades collagens (collagenases), laminins and as well as the cell adhesion molecules, growth factors and growth factor receptors through which they also influence the cellular signaling and function. Here, the degradation processes is modeled by kvw, where k is a positive constant. Moreover, ECM is not static, and it remodels continuously. In this work, we assume that the remodelling growth of ECM follows a logistic growth, that is, $\rho_v v\left(1 - \frac{u}{U} - \frac{v}{V}\right)$, where ρ_v is a positive constant. Eventually, the model equation for ECM is given by

$$\frac{\partial v}{\partial t} = -kvw + \rho_v v\left(1 - \frac{u}{U} - \frac{v}{V}\right) \qquad \text{in } \Omega\times(0, I). \tag{2.3}$$

Finally, the model for MDEs are considered. The MDEs are produced by cancer cells, and it is assumed to be diffuse throughout the tissues due to its random motion. Further, MDEs undergo some form of natural decay and also have a growth induced by cancer cells, and these processes are modelled by γw and $\zeta u\left(1 - \frac{w}{W}\right)$, respectively. Here, ζ is a positive constant and W is a reference MDE concentration. Hence, the model equation for MDE is given by

$$\frac{\partial w}{\partial t} = D_w\Delta w + \zeta u\left(1 - \frac{w}{W}\right) - \gamma w \qquad \text{in } \Omega\times(0, I), \tag{2.4}$$

where D_w is a constant diffusion coefficient of MDE.

2.2. Dimensionless form

Let $L = 0.1$ cm and $\tau = \frac{L^2}{D}$, (where $D \simeq 10^{-6}\,\mathrm{cm^2 s^{-1}}$) be the characteristic length and time scales, respectively. Using these characteristic and reference values, define the dimensionless variables as

$$\tilde{u} = \frac{u}{U}, \quad \tilde{v} = \frac{v}{V}, \quad \tilde{w} = \frac{w}{W}, \quad \tilde{x} = \frac{x}{L}, \quad \tilde{t} = \frac{t}{\tau}.$$

Applying these dimensionless variables to the system (2.2)–(2.4), and omitting the tilde afterwards, the dimensionless form of the Eqs. (2.2)–(2.4) in $\Omega\times(0, I)$ become:

$$\begin{aligned}
\frac{\partial u}{\partial t} - \nabla\cdot(d_1(u, v, w)\nabla u) + \nabla\cdot(\chi_u(v)u\nabla v) - \lambda u(1 - u - v) &= 0,\\
\frac{\partial v}{\partial t} + \eta vw - \rho v(1 - u - v) &= 0,\\
\frac{\partial w}{\partial t} - d_2\Delta w - \alpha u(1 - w) + \beta w &= 0.
\end{aligned} \tag{2.5}$$

where

$$\begin{aligned}
d_1(u, v, w) &= \tfrac{\tau D_u(u,v,w)}{L^2}, \quad & d_2 &= \tfrac{\tau D_w}{L^2}, \quad & \lambda &= \tau\mu, \quad & \chi_u(v) &= \tfrac{\chi_0(v)V\tau}{L^2},\\
\eta &= \tau kW, & \alpha &= \tau\zeta\tfrac{U}{W}, & \beta &= \tau\gamma, & \rho &= \rho_v\tau
\end{aligned}$$

are the dimensionless numbers.

In most of the previous studies, the cancer diffusion d_1 and the sensitivity function χ have been considered as constants or functions of space variables, see for example [7,10]. However, the cancer diffusion and the sensitivity function need not be constant always. Nevertheless, non-constant diffusion and sensitivity functions have been considered in some other cell migration models, that is, in models on wound healing, chemotaxis equations, glioblastoma, see for example [21,25,34,36]. Thus, we consider the following variants for the cancer diffusion function d_1:

For a constant $c > 0$,

*D*0: $d_1(u,v,w) = c$, represents that the random motility coefficient is constant.
*D*1: $d_1(u,v,w) = cw$, directly proportional to MDE consideration (it means that the random motility of cancer cell is high when there is a high concentration of MDE).
*D*2: $d_1(u,v,w) = c(1+uv)$, represents that increased cancer cell random movement towards the high density of region of cancer cells and ECM.
*D*3: $d_1(u,v,w) = \frac{c}{1+uv}$, denotes that decreased diffusion rate for an increased cancer cell density and ECM density and on the other way around.
*D*4: $d_1(u,v,w) = c + \frac{d_3 u^N}{a+u^N}$, where $a > 0, N > 0$ and $d_3 < 0$, suggests that diffusion is large when the amount of cells is small (the migrating tumor cells), but diffusion will be smaller when the cell density is large (the proliferating tumor cells).

Moreover, the following variants of the sensitivity function are also considered in this study: For a constant $\chi > 0$,

*H*0: Direct measurement: $\chi_u(v) = \chi$
*H*1: A logarithmic law: $\chi_u(v) = \frac{\chi}{1+v}$
*H*2: A receptor kinetic law: $\chi_u(v) = \frac{\chi}{(1+v)^2}$
*H*3: Michaelis-Menten kinetics: $\chi_u(v) = \frac{\chi v}{1+v}$
*H*4: Cooperative binding: $\chi_u(v) = \frac{2\chi v}{(1+v^2)^2}$.

2.3. Boundary and initial conditions

Under the assumption that the interactions of the cancer cells with ECM and the degradation of ECM by MDE takes place in an isolated system, the zero-flux type boundary conditions for the unknown space-time functions of the model are imposed, that is,

$$\xi \cdot (-d_1(u,v,w)\nabla u + \chi_u(v) u \nabla v) = 0 \quad \text{on} \quad \partial\Omega \times [0, I], \tag{2.6}$$

$$\frac{\partial w}{\partial \xi} = 0, \quad \text{on} \quad \partial\Omega \times [0, I], \tag{2.7}$$

where ξ is the outward normal vector on $\partial\Omega$. Further, the initial conditions

$$\begin{aligned} u_0 = u(x,0) &= \begin{cases} \exp(\frac{-r^2}{\epsilon}), & r \in [0, 0.25] \\ 0, & r \in (0.25, 1]. \end{cases} \\ v_0 = v(x,0) &= 1 - 0.5\ u(x,0), \\ w_0 = w(x,0) &= 0.5\ u(x,0), \quad \text{in } \Omega \end{aligned} \tag{2.8}$$

for the given system (2.5) with $\epsilon = 0.01$ and $r^2 = x_1^2 + x_2^2 + x_3^2$.

2.4. The parameter choice

The values for the parameters in (2.5) are needed for computations of the cancer invasion model. The values of these parameters are chosen from the literature and the experimental observations. Based to the theoretical and clinical studies, the dimensional values of the diffusion coefficients of the cancer density and the MDE concentration varies from 10^{-9} to $10^{-11}\,\mathrm{cm^2 s^{-1}}$ [6,7,10,33,39]. Further, the cancer cell proliferate rate lies between $0.02 - 0.72\,\mathrm{h}^{-1}$ [9,29,33,44] and the MDE decay rate varies from 2 s to 5 h [5,9,10]. Thus, the non-dimensional values of d_1 and d_2 are chosen between 10^{-5} and 10^{-3}. Moreover, the dimensionless range of λ and β are between 0.05 and 2. Due to the lack of experimental evidence, values of all other parameters are chosen as used in the literature. The used non-dimensional values of the parameters are $\chi \in [0.001, 1]$, $\eta \in [1, 20]$, $\rho \in [0.25, 4]$ and $\alpha \in [0.05, 1]$, see for more details [9,10,27].

3. Finite element scheme

In this section, we present a finite element scheme for the considered model. We consider the dimensionless form (2.5) of the cancer invasion mathematical model, and then derive the variational forms of the cancer cells density equation, the ECM density equation and the MDE concentration equation. After that, the spatial and temporal discretizations are presented.

3.1. Variational formulation

Let $L^2(\Omega)$ and $H^1(\Omega)$ denote the usual Lebesgue and Hilbert spaces, respectively, and $(\cdot,\cdot)$ denotes the inner product in $L^2(\Omega)$. Let $L^2(0, I, H^1(\Omega))$ be the solution space for the cancer cell density u, ECM density v and MDE concentration w. Now derive the variational form of the cancer invasion system (2.6) by multiplying each equation in the system by a test function $\phi \in H^1(\Omega)$, and integrate over Ω. After applying integration by parts to the higher order derivative terms and imposing the no flux boundary condition, the variational form of the system reads:

For given $u_0, v_0, w_0 \in L^2(\Omega)$ find $u, v, w \in L^2(0, I, H^1(\Omega))$ with $u' \in L^2(0, I, H^{-1}(\Omega))$ such that

$$\begin{aligned}
&\left(\frac{\partial u}{\partial t}, \phi\right) + a_u(u; u; v; w, \phi) = 0,\\
&\left(\frac{\partial v}{\partial t}, \phi\right) + a_v(v; v; u; w, \phi) = 0,\\
&\left(\frac{\partial w}{\partial t}, \phi\right) + a_w(w; u, \phi) = f(u, \phi),
\end{aligned} \tag{3.1}$$

for all $\phi \in H^1(\Omega)$, where

$$\begin{aligned}
a_u(u; \hat{u}; v; w, \phi) &= \int_\Omega d_1(u, v, w)\nabla u \cdot \nabla\phi\, dx - \int_\Omega \chi_u(v) u \nabla v \cdot \nabla\phi\, dx - \lambda \int_\Omega u(1 - \hat{u} - v)\phi\, dx,\\
a_v(v; \hat{v}; u; w, \phi) &= \eta \int_\Omega vw\phi\, dx - \rho \int_\Omega v(1 - u - \hat{v})\phi\, dx,\\
a_w(w; u, \phi) &= d_2 \int_\Omega \nabla w \cdot \nabla\phi\, dx + \int_\Omega w(\alpha u + \beta)\phi\, dx,\\
f(u, \phi) &= \int_\Omega \alpha u \phi\, dx.
\end{aligned}$$

Note that $u \in L^2(0, I, H^1(\Omega))$ and $u' \in L^2(0, I, H^{-1}(\Omega))$ implies that $t \mapsto u(t)$ as a mapping from $[0, I]$ into $L^2(\Omega)$ is continuous. Here $H^{-1}(\Omega)$ is the dual space of $H^1(\Omega)$.

3.2. Discrete problem

In this section, we first present the temporal discretization of the coupled variational system (3.1). In particular, the application of Crank–Nicolson time discretization is used for the system. Further, an iteration of fixed point type is developed to handle the nonlinear terms in the system. Moreover, the choice of the finite elements for the spatial discretization of the system (3.1) is also discussed.

3.2.1. Temporal discretization

Let $0 = t^0 < t^1 < \cdots < t^N = I$ be a decomposition of the considered time interval $[0, I]$, and $\delta_t = t^n - t^{n-1}, n = 1, \cdots, N$ denotes the uniform time step. Also, let $u^n(x) := u(x, t^n)$, $v^n(x) := v(x, t^n)$, $w^n(x) := w(x, t^n)$ be the semidiscrete solution at time t^n. After applying the implicit Crank–Nicolson discretization scheme, which is second order and A-stable, the semi-discrete (continuous in space) form of the system (3.1) reads:

For given u^{n-1}, v^{n-1} and w^{n-1} with $u^0 = u_0$, $v^0 = v_0$ and $w^0 = w_0$, find u^n, v^n, $w^n \in H^1(\Omega)$ such that

$$\begin{aligned}
&\left(\frac{u^n - u^{n-1}}{\delta_t}, \phi\right) + \frac{1}{2}a_u(u^n; u^n; v^n; w^n, \phi) = -\frac{1}{2}a_u(u^{n-1}; u^{n-1}; v^{n-1}; w^{n-1}, \phi),\\
&\left(\frac{v^n - v^{n-1}}{\delta_t}, \phi\right) + \frac{1}{2}a_v(v^n; v^n; u^n; w^n, \phi) = -\frac{1}{2}a_v(v^{n-1}; v^{n-1}; u^{n-1}; w^{n-1}, \phi),\\
&\left(\frac{w^n - w^{n-1}}{\delta_t}, \phi\right) + \frac{1}{2}a_w(w^n; u^n, \phi) = -\frac{1}{2}a_w(w^{n-1}; u^{n-1}, \phi) + f\left(\frac{u^n + u^{n-1}}{2}, \phi\right),
\end{aligned} \tag{3.2}$$

for all $\phi \in H^1(\Omega)$ and $n = 1, \cdots, N$.

3.2.2. Solution of the nonlinear system

In addition to the nonlinearity in the semi-discrete (continuous in space) form of the system (3.2), the coupling between the equations makes the computations more challenging. A fully implicit treatment of the nonlinear and coupled terms leads to a coupled, nonlinear algebraic system, and it will be very challenging to solve with a nonlinear solver. Contrarily, an explicit treatment of the nonlinear and coupled terms leads to a decoupled, linearized system. However, it may impose a severe restriction on the time step. Therefore, an iteration of fixed point type [18] is proposed to handle the nonlinear and coupled terms semi-implicitly.

Let us briefly explain the fixed point iteration steps for the nonlinear terms in the cancer density equation in the time interval (t^{n-1}, t^n). Let $u_0^n = u^{n-1}$, then the nonlinear integral terms in the cancer density equation are replaced with

$$\int_\Omega \chi_u(v_k^n) u_k^n \nabla v_k^n \cdot \nabla\phi \, dx \simeq \int_\Omega \chi_u(v_{k-1}^n) u_k^n \nabla v_{k-1}^n \cdot \nabla\phi \, dx; \qquad \int_\Omega u_k^n (1 - u_k^n - v_k^n)\phi \, dx \simeq \int_\Omega u_k^n (1 - u_{k-1}^n - v_{k-1}^n)\phi \, dx,$$

for $k = 1, 2, \ldots$. Further, we iterate until the residual of the linearized system becomes less than the prescribed threshold value (10^{-8}) or until the given maximal number of iterations. Finally, we set, $u^n = u_{k-1}^n$ and advance to the next time step. Using the above prescribed iteration of fixed point type, the linearized (semi-implicit) form of the semi-discrete system (3.2) reads:

For given $u_0^n = u^{n-1}$, $v_0^n = v^{n-1}$ and $w_0^n = w^{n-1}$, find u_k^n, v_k^n and w_k^n such that for all $\phi \in V$

$$\begin{aligned}
(u_k^n, \phi) + \frac{\delta_t}{2} a_u(u_k^n; u_{k-1}^n; v_{k-1}^n; w_{k-1}^n, \phi) &= (u^{n-1}, \phi) - \frac{\delta_t}{2} a_u(u^{n-1}; u^{n-1}; v^{n-1}; w^{n-1}, \phi), \\
(w_k^n, \phi) + \frac{\delta_t}{2} a_w(w_k^n; u_k^n, \phi) &= \delta_t f(\frac{u_k^n + u^{n-1}}{2}, \phi) + (w^{n-1}, \phi) - \frac{\delta_t}{2} a_w(w^{n-1}; u^{n-1}, \phi), \\
(v_k^n, \phi) + \frac{\delta_t}{2} a_v(v_k^n; v_{k-1}^n; u_k^n; w_k^n, \phi) &= (v^{n-1}, \phi) - \frac{\delta_t}{2} a_v(v^{n-1}; v^{n-1}; u^{n-1}; w^{n-1}, \phi),
\end{aligned} \tag{3.3}$$

for $k = 1, 2, \ldots$ and $n = 1, \cdots, N$. In computations, the fixed point iteration converges within two or three iterations for the prescribed residual threshold 10^{-8}, and the number of iterations increases when δ_t is increased.

3.2.3. Finite element discretization

Let Ω_h be a triangulation of Ω into tetrahedral cells. Suppose $V_h \subset H^1(\Omega)$ is a conforming finite element (finite dimensional) subspace of $H^1(\Omega)$ with basis functions $\{\phi_i\}$, $i = 1, 2, ..., \mathcal{N}$ such that $V_h = \text{span}\{\phi_i\}$, where $\mathcal{N}$ is the number of degrees of freedom. Further, define the finite element ansatz functions as

$$u_h^n(x) = \sum_{i=1}^{\mathcal{N}} u_i^n \phi_i(x), \quad v_h^n(x) = \sum_{i=1}^{\mathcal{N}} v_i^n \phi_i(x), \quad w_h^n(x) = \sum_{i=1}^{\mathcal{N}} w_i^n \phi_i(x).$$

Using the discrete form of the functions in (3.3) leads to a system of linearized (semi-implicit) system of algebraic equations

$$\begin{aligned}
\left(M + \frac{\delta_t}{2} A^u\right)\mathcal{U}^n &= \left(M - \frac{\delta_t}{2}\tilde{A^u}\right)\mathcal{U}^{n-1} \\
\left(M + \frac{\delta_t}{2} A^v\right)\mathcal{V}^n &= \left(M - \frac{\delta_t}{2}\tilde{A^v}\right)\mathcal{V}^{n-1} \\
\left(M + \frac{\delta_t}{2} A^w\right)\mathcal{W}^n &= \left(M - \frac{\delta_t}{2}\tilde{A^w}\right)\mathcal{W}^{n-1} + \delta_t\left(F + \tilde{F}\right),
\end{aligned} \tag{3.4}$$

where $\mathcal{U}^n = \text{vec}(\mathcal{U}^n)$, $\mathcal{V}^n = \text{vec}(\mathcal{V}^n)$ and $\mathcal{W}^n = \text{vec}(\mathcal{W}^n)$ are the vectorization of the solution matrices $\mathcal{U}^n = [u_j^n]$, $\mathcal{V}^n = [v_j^n]$, and $\mathcal{W}^n = [w_j^n]$, respectively. Further, we denote the fully discrete solutions by $u_{h,k}^n$, $v_{h,k}^n$ and $w_{h,k}^n$ at a fixed point step $k = 1, 2, \ldots$. In the system (3.4), the entries of the mass, stiffness matrices and the source vector at a fixed point iteration step k are given by

$$\begin{aligned}
[M]_{ij} &= \int_{\Omega_h} \phi_i(x)\ \phi_j(x)\, dx, \\
[A^u]_{ij} &= \int_{\Omega_h} d_1(u_{h,k-1}^n, v_{h,k-1}^n, w_{h,k-1}^n)\nabla\phi_i(x) \cdot \nabla\phi_j(x)\, dx - \int_{\Omega_h} \chi_u(v_{h,k-1}^n)\ \phi_i(x)\ \nabla v_{h,k-1}^n \cdot \nabla\phi_j(x)\, dx \\
&\quad -\lambda \int_{\Omega_h} \phi_i(x)\ (1 - u_{h,k-1}^n - v_{h,k-1}^n)\ \phi_j(x)\, dx, \\
[\tilde{A^u}]_{ij} &= \int_{\Omega_h} d_1(u_h^{n-1}, v_h^{n-1}, w_h^{n-1})\nabla\phi_i(x) \cdot \nabla\phi_j(x)\, dx - \int_{\Omega_h} \chi_u(v_h^{n-1})\phi_i(x)\ \nabla v_h^{n-1} \cdot \nabla\phi_j(x)\, dx \\
&\quad -\lambda \int_{\Omega_h} \phi_i(x)\ (1 - u_h^{n-1} - v_h^{n-1})\ \phi_j(x)\, dx, \\
[A^v]_{ij} &= \eta \int_{\Omega_h} \phi_i(x)\ w_{h,k}^n\ \phi_j(x)\, dx - \rho \int_{\Omega_h} \phi_i(x)\ (1 - u_{h,k}^n - v_{h,k-1}^n)\ \phi_j(x)\, dx, \\
[\tilde{A^v}]_{ij} &= \eta \int_{\Omega_h} \phi_i(x)\ w_h^{n-1}\ \phi_j(x)\, dx - \rho \int_{\Omega_h} \phi_i(x)\ (1 - u_h^{n-1} - v_h^{n-1})\ \phi_j(x)\, dx,
\end{aligned}$$

$$[A^w]_{ij} = d_2 \int_{\Omega_h} \nabla\phi_i(x) \cdot \nabla\phi_j(x)\, dx + \int_{\Omega_h} \phi_i(x)\ (\alpha u^n_{h,k} + \beta)\ \phi_j(x)\, dx,$$

$$[\widetilde{A^w}]_{ij} = d_2 \int_{\Omega_h} \nabla\phi_i(x) \cdot \nabla\phi_j(x)\, dx + \int_{\Omega_h} \phi_i(x)\ (\alpha u^{n-1}_{h} + \beta)\ \phi_j(x)\, dx,$$

$$[F]_i = \alpha \int_{\Omega_h} u^n_{h,k}\ \phi_i(x)\, dx,$$

$$[\widetilde{F}]_i = \alpha \int_{\Omega_h} u^{n-1}_{h}\ \phi_i(x)\, dx.$$

4. Numerical experiments

We first present a convergence study to show the optimal order of convergence of the proposed finite element scheme. Next, a mesh convergence analysis for the discrete cancer system (3.4) is performed to obtain a grid independent solution. Further, the proposed finite element scheme is validated for the considered cancer invasion model using the existing numerical results presented in [17]. Moreover, an array of simulations are performed to study the effects of different density-dependent nonlinear diffusion functions and haptotactic sensitive functions in an unit cube and realistic geometries.

The numerical scheme is implemented in our in-house finite element package ParMooN, and the system of algebraic equations are solved using UMFPACK [13,14]. Computations are performed using Intel(R) Core(TM) i7-3770s CPU with 3.10 GHZ and 8GB RAM.

4.1. Convergence study

To perform the convergence analysis of the proposed numerical scheme, consider a sufficiently smooth solution for the following cancer invasion coupled model

$$\begin{aligned} \frac{\partial u}{\partial t} - \nabla\cdot(d_1(u,v,w)\nabla u) + \nabla\cdot(\chi_u(v)u\nabla v) - \lambda u(1-u-v) &= f_u \quad \text{in } (0,1)^3\times(0,I),\\ \frac{\partial v}{\partial t} + \eta v w - \rho v(1-u-v) &= f_v \quad \text{in } (0,1)^3\times(0,I),\\ \frac{\partial w}{\partial t} - d_2\Delta w - \alpha u(1-w) + \beta w &= f_w, \quad \text{in } (0,1)^3\times(0,I). \end{aligned} \tag{4.1}$$

Here, the source terms f_u, f_v, f_w, initial and non-homogeneous Dirichlet boundary values are chosen such that the solution of the system (4.1) is

$$u = e^{-kt}\sin(\pi x)\cos(\pi y)\cos(\pi z), \quad v = e^{-kt}\sin(\pi x)\sin(\pi y)\sin(\pi z), \quad w = e^{-kt}\cos(\pi x)\sin(\pi y)\sin(\pi z).$$

For this test example, an array of computations with different levels of meshes and spatial discretizations on $\Omega = [0,1]^3$ are performed. The three-dimensional domain Ω is decomposed into hexahedral cells and trilinear finite elements are used. The initial mesh level consists of 27 degrees of freedom (unknown solution coefficients) for each unknown u, v, w with the mesh size $h = 0.866025$. Further, the successive levels of meshes are obtained by uniformly refining the initial coarse mesh. Computations are performed up to the level, in which the number of degrees of freedom is 35937 and the mesh size $h = 0.0541265$. Further, the numerical errors are computed using

$$E_1 := l^\infty\big(0, I; L^2(\Omega)\big) = \sup_{n=1,\cdots,N} \| u(t^n) - u_h(t^n)\|_{L^2(\Omega)}$$

$$E_2 := l^2\big(0, I; L^2(\Omega)\big) = \left(\sum_{n=1}^{N} \delta_t\ \| u(t^n) - u_h(t^n)\|^2_{L^2(\Omega)}\right)^{1/2}.$$

Moreover, the following two cases are considered in order to perform the convergence study:

(i) Q_1 finite elements with backward Euler time discretization with $\delta_t \propto h^2$
(ii) Q_1 finite elements with Crank–Nicolson time discretization with $\delta_t \propto h$

The obtained numerical errors in both cases are presented in Fig. 1. Plots (a) and (b) in the first row of the Fig. 1 represent the $l^\infty(0, I; L^2(\Omega))$ error in logarithmic scale obtained with the backward Euler (case i) and the Crank–Nicolson scheme (case ii), respectively. Similarly, the next two plots (c) and (d) represent the $l^2(0, I; L^2(\Omega))$ error in logarithmic scale obtained with backward Euler (case i) and Crank–Nicolson scheme (case ii), respectively . These plots show the optimal order of convergence order (two) in both time discretization cases with the trilinear hexahedral (Q_1) finite element.

4.2. Grid independence test and validation

Grid independence test is one of the standard numerical study used to obtain a mesh independent solution. Further, it evaluates the robustness and accuracy of the numerical scheme. In order to perform the grid independence study for the

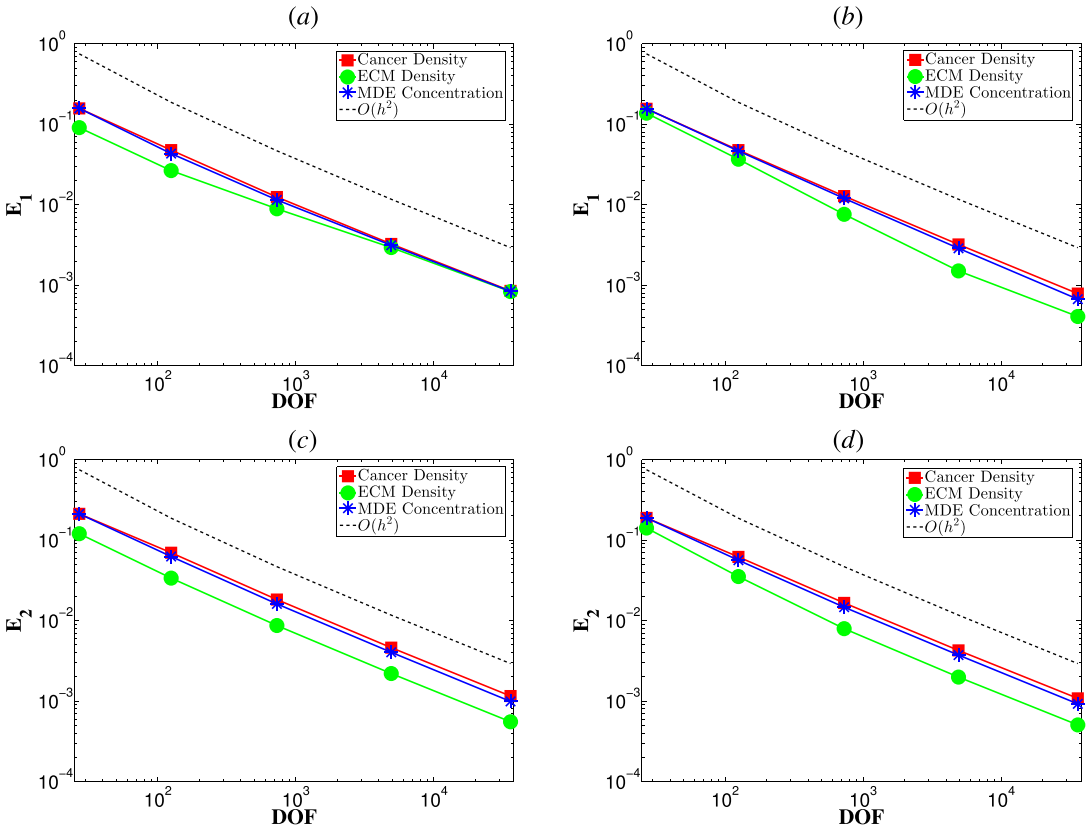

Fig. 1. Error plots for the order of convergence shows the logarithmic value of $l^\infty(0, I; L^2(\Omega))$ and $l^2(0, I; L^2(\Omega))$ norms of the error for backward Euler and Crank–Nicolson scheme respectively against the increasing logarithmic value of the degrees of freedom (DOF).

proposed finite element scheme, the following dimensionless parameters of model are considered:

$$c = 0.0001, \quad d_2 = 0.0005, \quad \lambda = 0.75, \quad \chi = 0.005,$$
$$\eta = 10, \quad \rho = 1.5, \quad \alpha = 0.25, \quad \beta = 0.10$$

Computations are performed in the domain $[0, 1]^3$ with the initial and boundary conditions (2.6). Moreover, the initial mesh level ($L0$) consists of 729 degrees of freedom (unknown solution coefficients) for each unknown variable with the mesh size, $h = 0.2165064$. The successive mesh levels ($L1$, $L2$ and $L3$) are obtained by refining the initial mesh uniformly. The final mesh level, $L3$ consists of 274,625 degrees of freedom for each unknowns, totally, 823,875 degrees of freedom with $h = 0.02706325$.

The numerically obtained finite element solutions are depicted in Fig. 2. To visualize the grid independence behaviour better, the cancer cell density, ECM density and MDE concentration at $t = 10$ with mesh levels $L0$ to $L3$ are plotted in Fig. 2. Qualitative difference in pattern morphology of each solution can clearly be observed in Fig. 2. The first row in Fig. 2(i) represents the cancer cell density obtained with L0, L1 and L2 meshes at time $t = 10$, whereas the second and third rows of the Fig. 2((ii) and (iii)) show the ECM density and the MDE concentration, respectively. The evolution of the cancer cell density and its interacting with ECM by producing MDE can clearly be seen in Fig. 2. Since the proliferation rate of cancer cells is high ($\lambda = 0.75$), the growth of the cancer cell is also more. In addition to the cancer growth, the haptotaxis effect accelerates the invasion of cancer cells into the ECM. The process of invasion can also clearly be seen in Fig. 2, and it is achieved through the production of more MDE by the cancer cells, see the third row, Fig. 2(iii).

In the coarser mesh level $L0$, the regular spot pattern of each solution breaks down, and it becomes stable in the finer mesh level. The solutions obtained with $L2$ and $L3$ meshes are almost identical, and it shows that a mesh with $h = 0.0541265$ is sufficient for a mesh independent solution for the considered model and parameters. Therefore, the $L2$ mesh is used in all our further computations where it consists of 32,768 degrees of freedom for each unknown variable, that is, 98,304 degrees of freedom all together in the considered model.

Next, the computed three-dimensional numerical solution is compared with the numerical results published in [17], in order to validate the proposed finite element scheme for the tumor migration model. In the validation test example, the same dimensionless values as in [17] are used, that is,

$$c = 0.0001, \quad d_2 = 0.0005, \quad \lambda = 0.75, \quad \chi = 0.00005, \quad \eta = 10, \quad \rho = 0.0, \quad \alpha = 0.1, \quad \beta = 0.$$

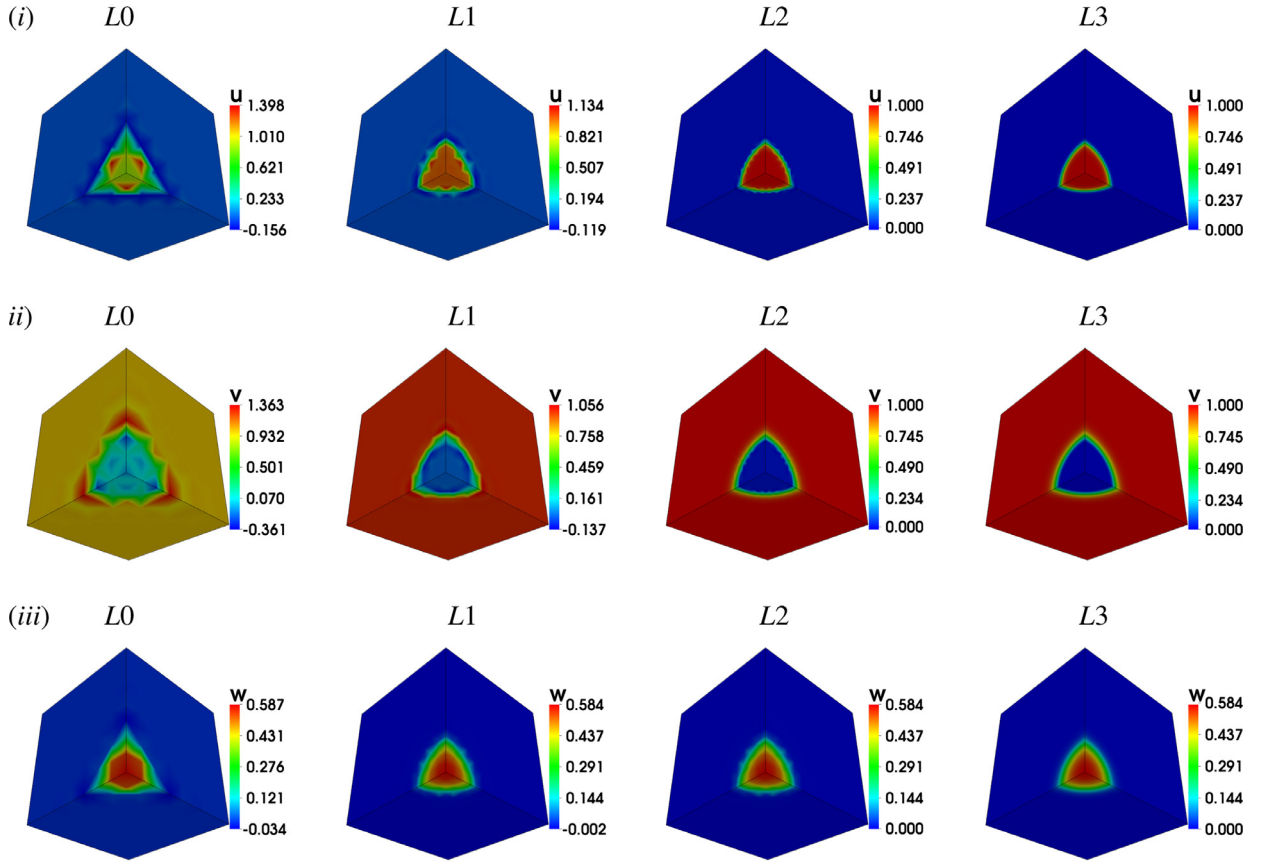

Fig. 2. Evolution of the cancer cell density, ECM density and MDE concentration with the dimensionless time instance $t = 10$ and obtained with different mesh levels for the mess convergence study.

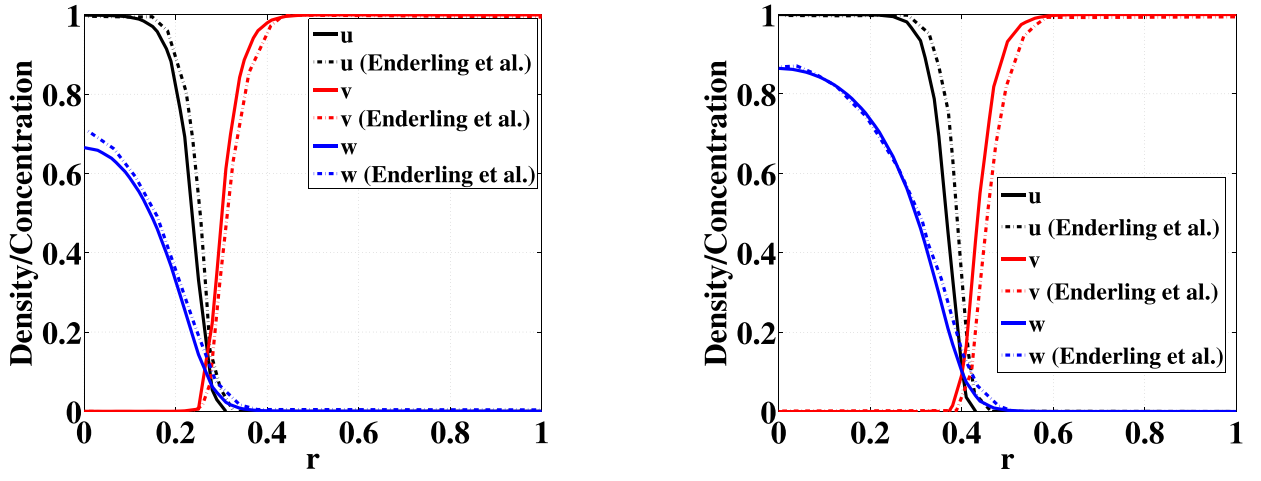

Fig. 3. Comparison of the evolution of the cancer cell density, ECM density and MDE concentration at different instances $t = 10$ and $t = 20$. The dashed lines are the FEM solution and the dotted lines are the solutions represented in Enderling et al. [17].

A 3D finite element computation is performed in the unit cube domain with *L2* mesh, and the cancer cell density, ECM density and MDE concentration over the line $y = 0$ and $z = 0$ are plotted in Fig. 3. The obtained results are consistent with results in [17]. The continuous dashed lines denote the finite element solution, whereas the dotted lines are the solutions reported in [17]. The finite element solutions, the density of cancer cells, ECM density and concentration of MDE are in good agreement both qualitatively and quantitatively with the solutions reported in [17].

4.3. Effects of nonlinear diffusion functions

The cancer cells become more aggressive during the growth and migration of a solid tumour, and consecutively it initiates the migration of cancer cells to other organs of the body. Therefore, the effects of the density-dependent nonlinear diffusion with various diffusion rates, ($D0 - D4$) described in the Section 2 are studied here. The numerical results are obtained using the parameter values:

$$c = 0.001, \quad d_2 = 0.001, \quad \lambda = 0.5, \quad \chi = 0.005, \quad \eta = 10, \quad \rho = 0.1, \quad \alpha = 0.25, \quad \beta = 0.1$$

Further, the haptotaxis function $\chi_u(v)$ is assumed as a direct measurement, that is, a constant function in this study. All numerical simulations are performed until the dimensionless end time $I = 20$ with the time step $\delta_t = 0.1$. Further, the computational mesh $L2$ is same as in the previous example. It should be emphasized that the number of fixed point iterations is just one or two for the examples considered in the cube geometry.

The computationally obtained numerical results of the cancer density with different diffusion functions at various time instances, $t = 5, 10, 15, 20$ are depicted in Fig. 4. Apart from the growth the diffusion rate is also inducing the migration of cancer cells. So the results obtained with the constant diffusion model $D0$ (first row (i) in Fig. 4) are compared with different diffusion models. In the diffusion model $D1$, the random motility is directly proportional to the MDE concentration. The obtained results at different instances $t = 5, 10, 15, 20.$ are depicted in the second row of Fig. 4(ii). It can clearly be seen that a part of the cancer cells break away from the main body of the tumour at $t = 5$. This effect resulted into two distinct group of cancer cells and both of them migrates further into the ECM domain at $t = 10$. A similar behaviour is resumed even after $t = 10$, that is, at the dimensionless time $t = 15$ and 20, see Fig. 4(ii). These kind of effects result into the metastasis behaviors of the cancer cells. Next, let us consider the diffusion models $D2$ and $D3$. In the model $D2$, the random motility is high towards the large population of cancer cells and ECM, whereas the random motility rate decreases when the population of the cancer cells and ECM increase and vice versa in the model $D3$. We can observe from the snapshots in Fig. 4(iii) and (iv) that the pattern morphology obtained with $D2$ and $D3$ diffusion models are almost identical. The invasion profile of cancer cells is very similar in the diffusion models $D2$ and $D3$, where a part of the cancer cells move into the ECM domain from the main body of tumour and then diffuse slowly, see Fig. 4(iii) and (iv).

Finally, the random motility function $D4$ is considered. In this example, $d_3 = -0.000999$, $a = 10^{16}$, $N = 2$ and $c = 0.001$ are used. As expected, the cancer cells migrate from the main body of the tumour into the ECM domain, see Fig. 4(v). Even though the migration profile of cancer cells look similar in all diffusion models, the cancer density (u) obtained with $D4$ model varies from all other diffusion models. Further, we can also observe that the morphological changes of cancer cells with constant diffusion rate, Fig. 4(i)) is highly comparable with the patten provided by the nonlinear diffusion models such as $(D2) - (D4)$, Fig. 4($iii - v$)) except the case ($D1$), Fig. 4(ii). Note that the cancer cells are considered as two differing populations in this test case. The proliferate cells are diffuse slowly but grow as fast as possible. At the same time, migrating cells are diffuse quickly, invade the distance as far as possible, but do not resume rapid growth on the density.

4.4. Effects of various haptotactic functions

The influence of haptotactic function on the spatio-temporal dynamics of the cancer invasion is studied in this section. To get an insight into the haptotaxis mechanism, numerical simulations are performed with a variety of nonlinear haptotactic sensitivity functions. The considered haptotactic models are $H0 - H4$ that are described in Section 3. The obtained numerical results with different haptotactic models are compared with the results of constant haptotactic sensitivity function, H_0. In all these simulations, the haptotactic rate χ is used as 0.05, whereas all other parameters are chosen as in the previous Section 4.3. Snapshots of the cancer cell migration towards the ECM domain and the degradation of ECM by the production of MDEs are presented in Fig. 5–7 at different time instances, $t = 5, 10, 15, 20$. It can clearly be observed that the morphological changes in the cancer cells is influenced by the variation in haptotactic sensitivity function, see Figs. 6 and 7. Further, the cancer cells migrate in the direction of increasing density gradient of the haptoattractant ECM.

In the case of $H1$, the haptotactic sensitivity rate of the cancer cells increases when the ECM density decreases. Thus, the population of the cancer cells reduces from its initial level and a portion of the cancer cells starts migrating towards the gradient direction of the ECM domain, see the snapshot at $t = 5$, in Fig. 6. Eventually, the cancer cells degrade the ECM by producing more MDEs during the tumour invasion, see the first snapshot in the second row of Fig. 6. Moreover, this invading portion of cancer cells moved towards the direction of the gradient of the haptoattractant ECM and reaches the boundary of the domain, see the last snapshots in the first and second row of Fig. 6.

Next, consider the model $H2$, a receptor-kinetic law for haptotactic sensitive function $\chi(v)$, which is the most commonly used form in the chemotaxis type equations. In this type of model, the receptors may become fully occupied when the density of the ECM is high, and hence the cancer cells will not be able to migrate into ECM further. The numerical results for this model are depicted in the Fig. 6(iii) and (iv). The observed pattern morphology of the cancer density and ECM density in the model $H2$ is indistinguishable with the results obtained with the $H1$ model, see Fig. 6. We can observe that the invasion patterns of cancer cells on ECM domain with nonlinear haptotaxis models, $(H1) - (H2)$, are similar to the pattern produced by the constant haptotactic model $H0$.

We next discuss the results obtained with the realistic form of receptor-kinetic law such as cooperative binding form ($H3$), and the Michaelis-Menten kinetic model ($H4$). In both test cases, as expected the cancer cells migrate towards the

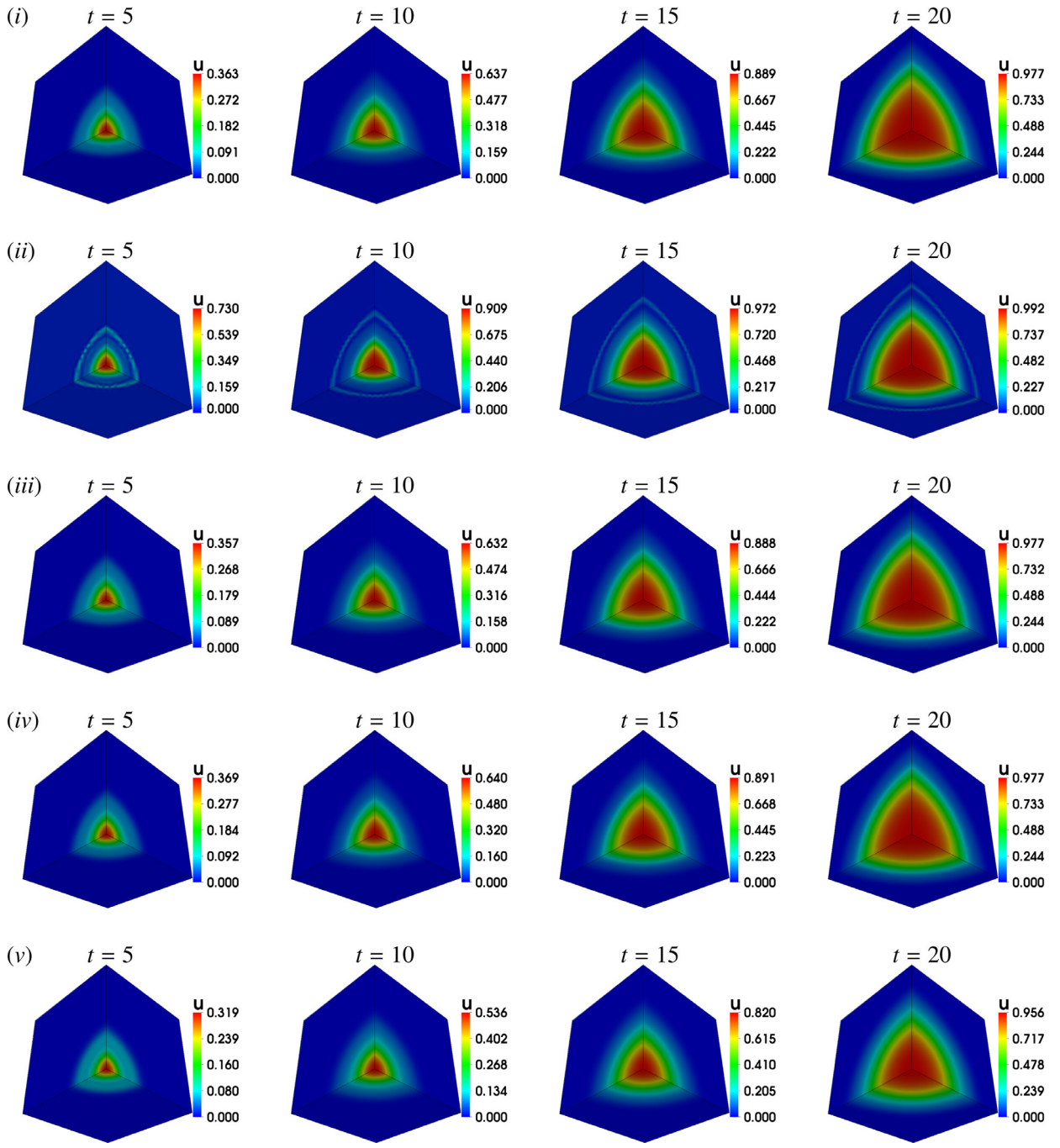

Fig. 4. Sequence of images in rows, $(i) - (v)$, show the effects of various nonlinear density-dependent diffusion functions, $(D0) - (D4)$, respectively, on the cancer cell density at different instances $t = 5,\ 10,\ 15,\ 20$ with dimensionless cancer density diffusion value $c = 0.001$. All other parameters are of the model (2.5) are fixed as in the Section 4.3.

gradient direction of ECM domain, and MDEs produced by the cancer cells degrade the ECM, see Fig. 7. However, the pattern morphology of these models, $(H3) - (H4)$, (see Fig. 7) is not identical to the pattern induced by the models $(H0) - (H2)$ (see Figs. 5 and 6). Further, the results in Figs. 6 and 7 confirm that the invasion is a dominant process than proliferation of the cancer cells when there is a high haptotactic rate. These results clearly specify the importance of the haptotaxis effects in cancer invasion and shows its role in the metastasis behaviors of the cancer cells.

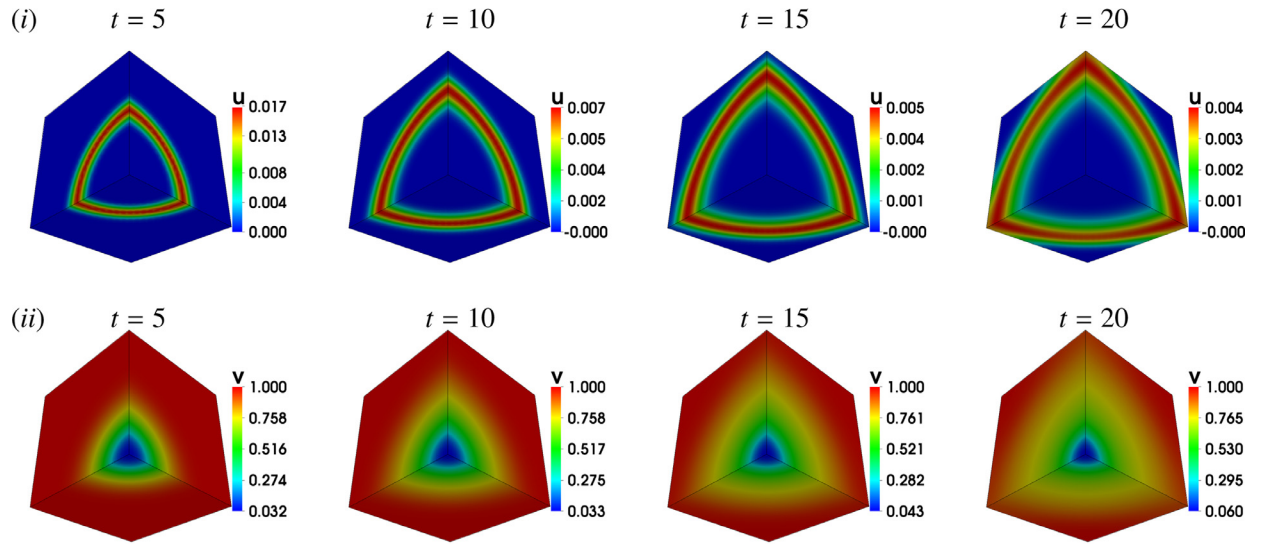

Fig. 5. Sequence of images show the effects of direct measurement form of haptotactic sensitivity function on cancer cell density and ECM density at different dimensionless time instances $t = 5,\ 10,\ 15,\ 20$ with the haptotactic constant value $\chi = 0.05$. All other parameters are of the model (2.5) fixed as in Section 4.4.

5. Cancer invasion in the realistic-geometry

In this section, we consider a realistic spatial geometry for the cancer invasion model (2.5), that is, invasion of cancer in a realistic breast geometry is considered. This geometry is obtained using MR-images as in [8] and triangulated using atlas mesh generator. Since the metastasis cancer invasion model is considered in this work, the tumor is allowed to invade the outer boundary of the domain, that is, the skin [28]. Further, the fat region of the breast tissue and the assumed initial values of the cancer cell density, ECM density and MDE concentration on the realistic domain are shown in Fig. 8. Note that the images of u, v and w in Fig. 8 are the iso surface view of the original three-dimensional breast geometry. Further, the number of fixed point iteration steps is less than five in all computations performed on the realistic geometry.

5.1. Grid independence test on the realistic-geometry

We perform the grid independence study on the realistic geometry with the following parameters:

$$c = 0.001, \quad d_2 = 0.005, \quad \lambda = 0.25, \quad \chi = 0.005, \quad \eta = 10, \quad \rho = 0.25, \quad \alpha = 0.75, \quad \beta = 0.15$$

Computations are performed until the dimensionless end time $I = 10$ with the time step $\delta_t = 0.1$. In the grid independence test, the initial mesh level ($B0$) consists of 31,910 vertices and 173,101 tetrahedral cells with minimum mesh size $h = 1.77878$ and maximum mesh size $h = 6.16232$. The next mesh level ($B1$) consists of 242,728 vertices and 1,384,808 tetrahedral cells with minimum mesh size $h = 0.8893905$ and maximum mesh size $h = 4.223773$. The final mesh level ($B2$) consists of 1,893,495 vertices and 11,078,464 tetrahedral cells with minimum mesh size $h = 0.4446952$ and maximum mesh size $h = 2.111886$. Computational results obtained with these mesh levels are depicted in the Fig. 9 at the dimensionless time $t = 10$. The first row in Fig. 9 represents the cancer density, ECM density and MDE concentration, respectively, over the line r through the centre of the tumor in the mesh levels $B0$, $B1$ and $B2$ at $t = 10$. Further, the second row of the Fig. 9 represents the closure look of the corresponding figures in the first row. Even though, the difference between the solutions obtained by each mesh level is very small, a closure look at these plots clearly shows the mesh behavior, see, Fig. 9 (second row). It shows that the solutions obtained with $B1$ and $B2$ meshes are almost identical and therefore, mesh level consists of minimum of $h = 0.8893905$ is sufficient for mesh independent solution. Thus, the $B1$ mesh level is used for all simulations in realistic geometry.

5.2. Effects of nonlinear functions on realistic geometry

The evolution of tumor proliferation and invasion on the realistic domain are investigated for different diffusion and the hapotactic sensitive models. It is observed in the previous sections that various nonlinear diffusion and haptotactic functions induce different morphology pattern in the cancer invasion model. Therefore, it is essential to study the effects of nonlinear diffusion and haptotactic sensitive functions in the considered realistic geometry. In particular, the nonlinear diffusion ($D1$) and the haptotactic sensitivity function ($H3$) provide a distinct sequence of cancer cell migration towards the ECM domain. Therefore, we consider the cancer invasion model with combinations of above mentioned models.

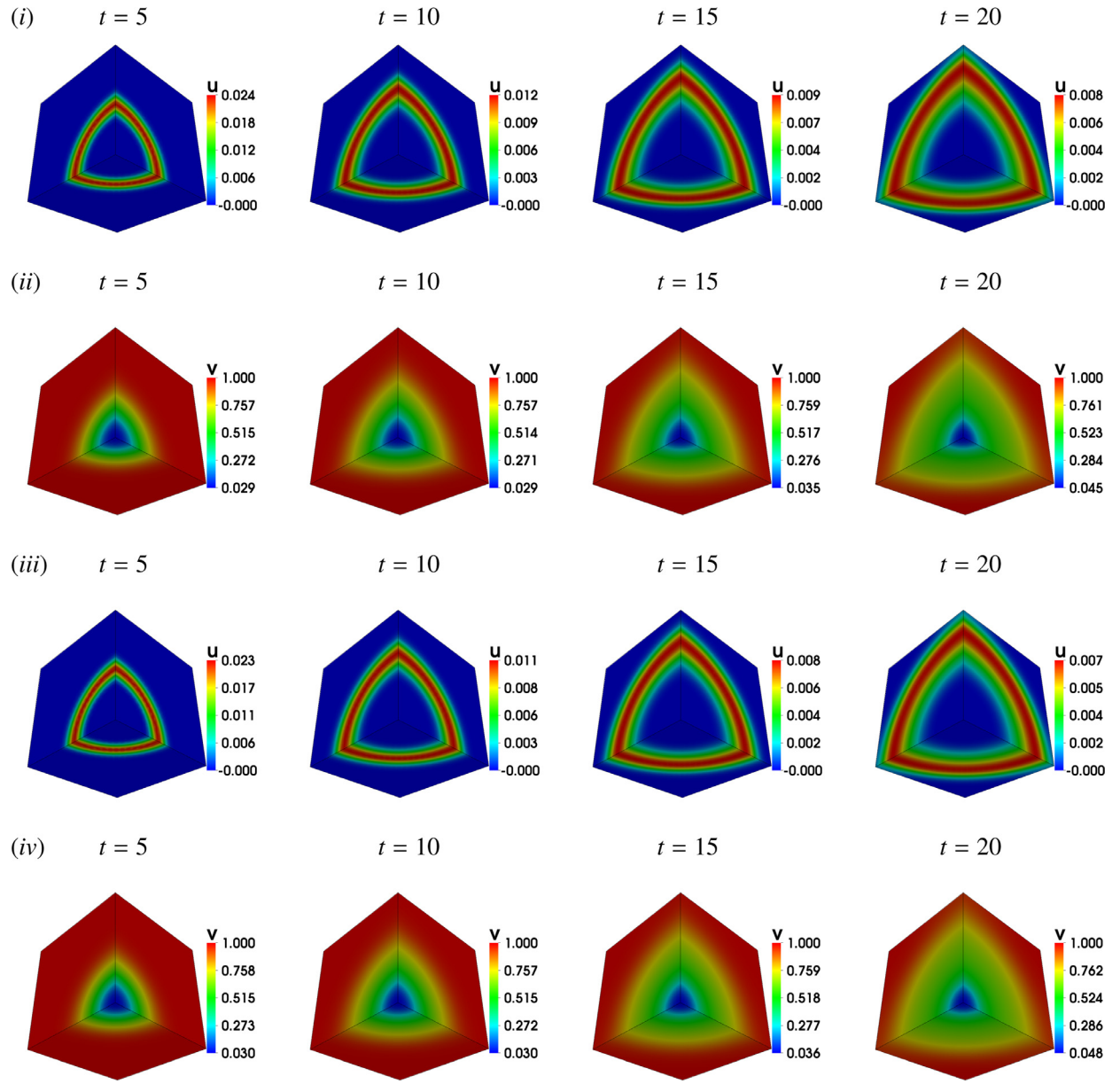

Fig. 6. Sequence of images show the effects of logarithmic (first two rows) and receptor kinetic (last two rows) forms of haptotactic sensitivity function on cancer cell density and ECM density at different dimensionless time instances $t = 5,\ 10,\ 15,\ 20$ with the haptotactic constant value $\chi = 0.05$. All other parameters are of the model (2.5) fixed as in Section 4.4.

In this study, the following four variants are considered:

(a) diffusion model ($D0$) with haptotactic sensitive model ($H0$)
(b) diffusion model ($D0$) with haptotactic sensitive model ($H3$)
(c) diffusion model ($D1$) with haptotactic sensitive model ($H0$)
(d) diffusion model ($D1$) with haptotactic sensitive model ($H3$)

Further, the computationally obtained numerical results of the cancer cell density (u) at different dimensionless time instances, $t = 40, 80, 120$ and 200, are presented in Figs. 10–14.

In the first case (a), we initially assumed that the cancer cells proliferation rate $\lambda = 0.25$ and the haptotactic rate $\chi = 0.005$ and all other parameters are fixed as in the Section 5.1. Sequence of images in Fig. 10(i) clearly show the effects of the cancer cells proliferation and the cell migration towards ECM on the realistic geometry. Initial density of the cancer cells are described as the spherical shape (using Gaussian distribution) and the high density of the cancer cells are pictured in the

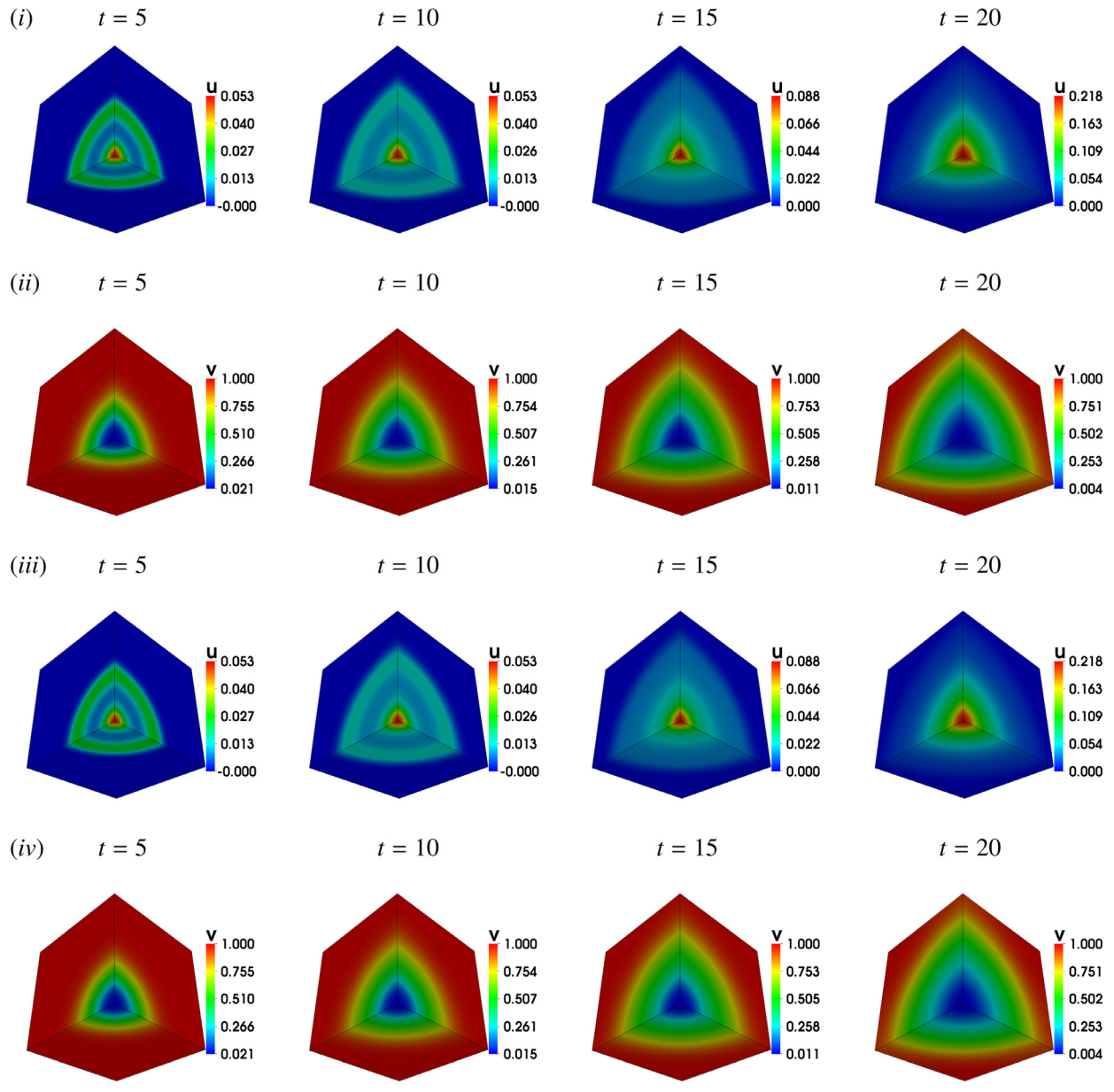

Fig. 7. Sequence of images show the effects of Michaelis-Menten kinetics (first two rows) and cooperative binding (last two rows) forms of haptotactic sensitivity functions on cancer cell density and ECM density at different dimensionless time instances $t = 5,\ 10,\ 15,\ 20$ with the haptotactic constant value $\chi = 0.05$. All other parameters are of the model (2.5) fixed as in Section 4.4.

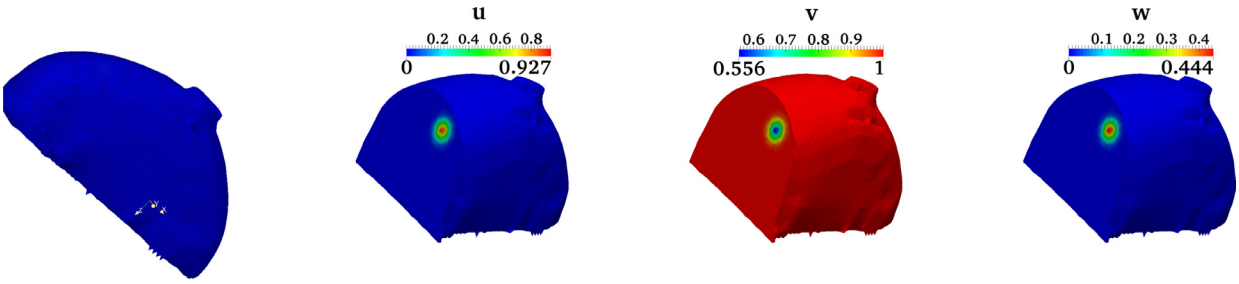

Fig. 8. Sequence of images show the mesh, the initial values of the cancer density, ECM density and MDE concentrations in the breast geometry.

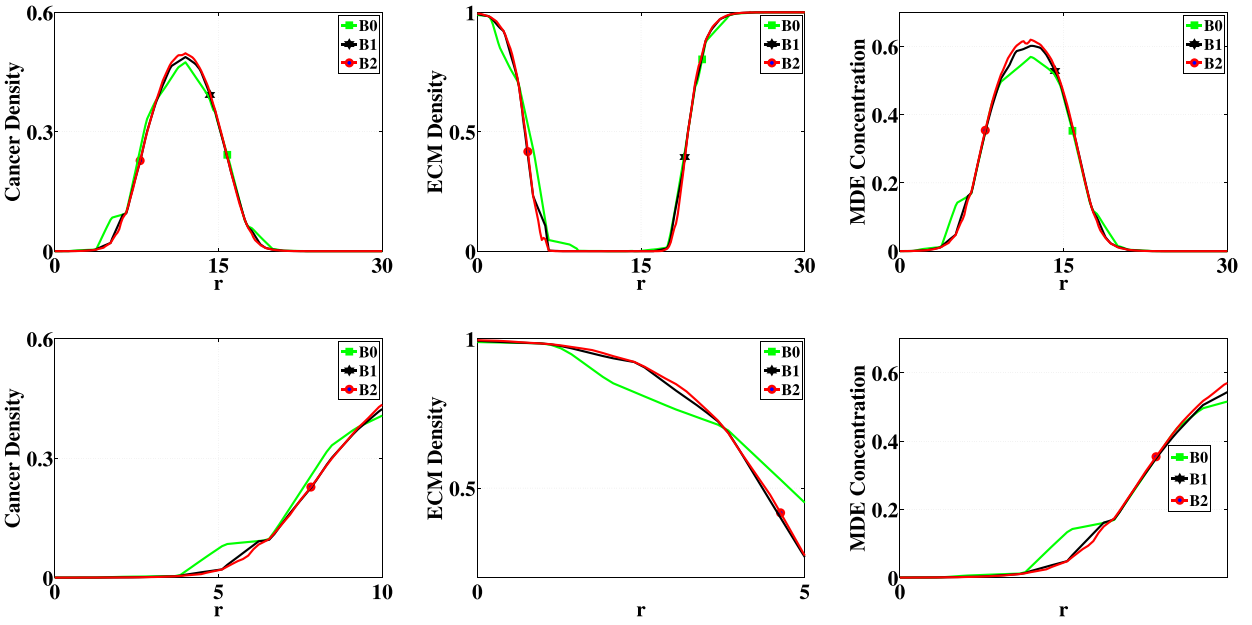

Fig. 9. Evolution of the cancer cell density, ECM density and MDE concentration at time $t = 10$, obtained with different mesh levels. The second row is the closure look of the first row at time $t = 10$.

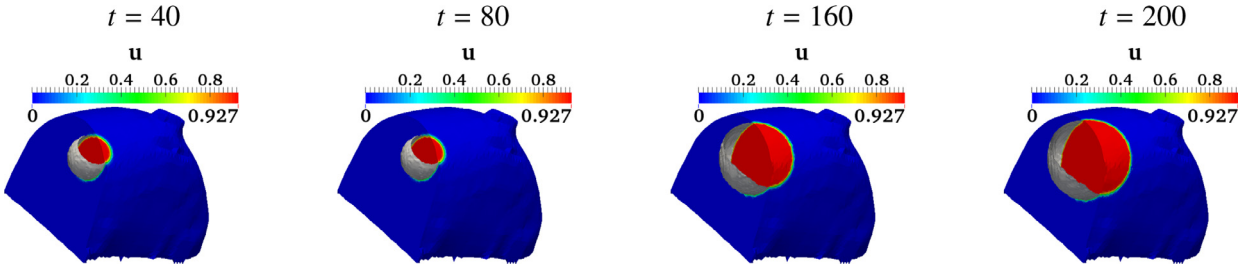

Fig. 10. Sequence of images show the cancer density in the test case (a) at different dimensionless time instances $t = 40,\ 80,\ 160,\ 200$ for different values of model parameters as chosen in the Section 5.1.

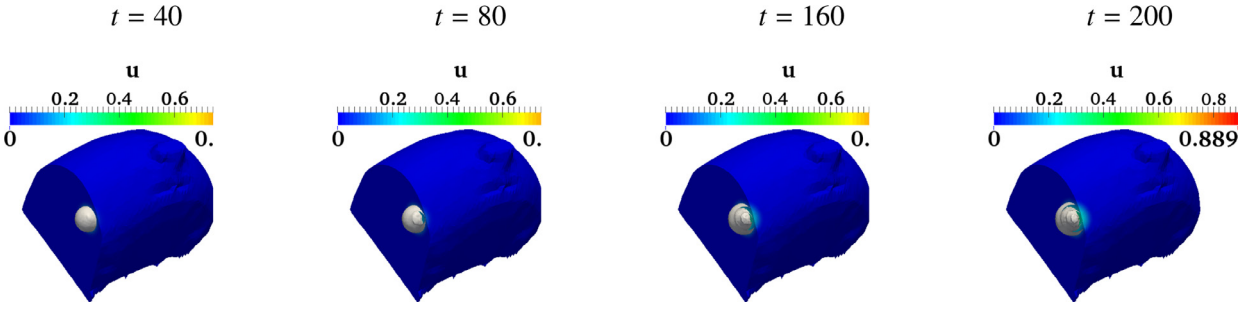

Fig. 11. Sequence of images show the cancer density in the test case (a) with increased haptotaxis rate ($\chi = 0.05$) and decreased proliferation rate ($\lambda = 0.01$) at different dimensionless time instances $t = 40,\ 80,\ 160,\ 200$ for different values of model parameters as chosen in the Section 5.1.

core of the sphere whereas the density reduces exponentially form core of the sphere. The rest of the space in the breast domain coordinates corresponds to zero cancer density. Since $v = 1 - u$, the density of ECM is exponentially increasing around the sphere and the remaining portion of breast domain other than the cancer density sphere is completely covered with matrix components, see Fig. 8.

As we can observe in Fig. 10(i), the density of cancer cells increases rapidly from the initial level due to the effect of logistic proliferation. Further, we noticed that the cancer cells become more malignant and invaded approximately one third of the ECM domain at end time $t = 200$ from the initial occurrence of cancer, see Fig. 10. This invasion is mainly occurred due to the assumption of a moderate growth rate ($\lambda = 0.25$) for the cancer cells.

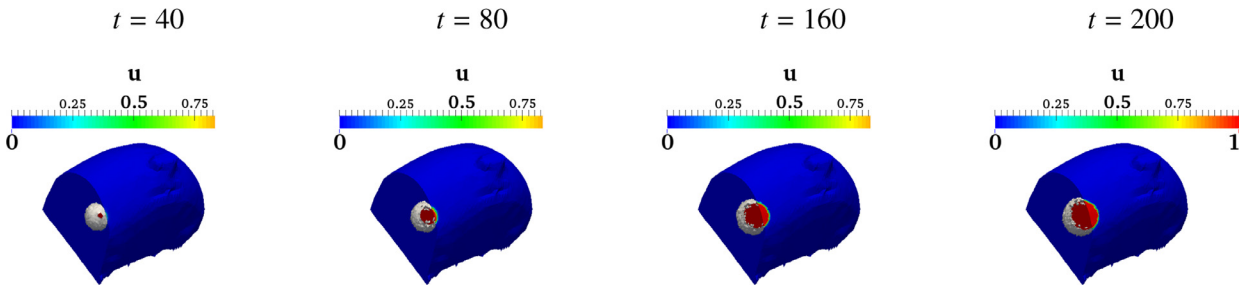

Fig. 12. Sequence of images show the cancer density obtained with the test case (b) at different dimensionless time instances $t = 40,\ 80,\ 160,\ 200$ for different values of model parameters as chosen in the Section 5.1.

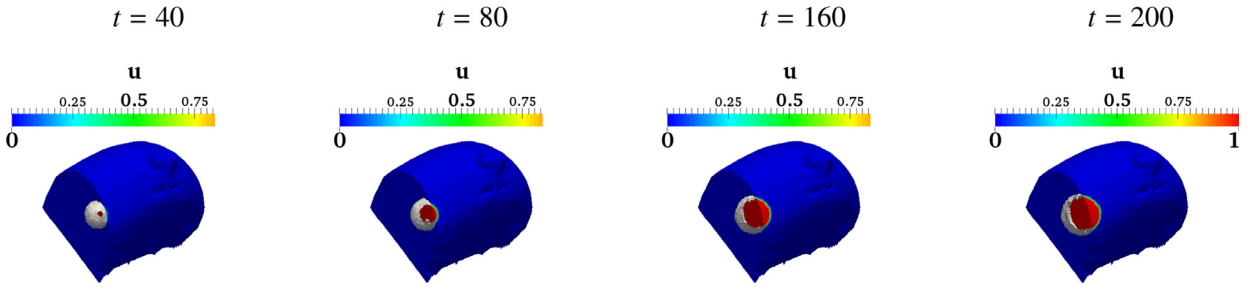

Fig. 13. Sequence of images show the cancer density obtained with the test case (c) at different dimensionless time instances $t = 40,\ 80,\ 160,\ 200$ for different values of model parameters as chosen in the Section 5.1.

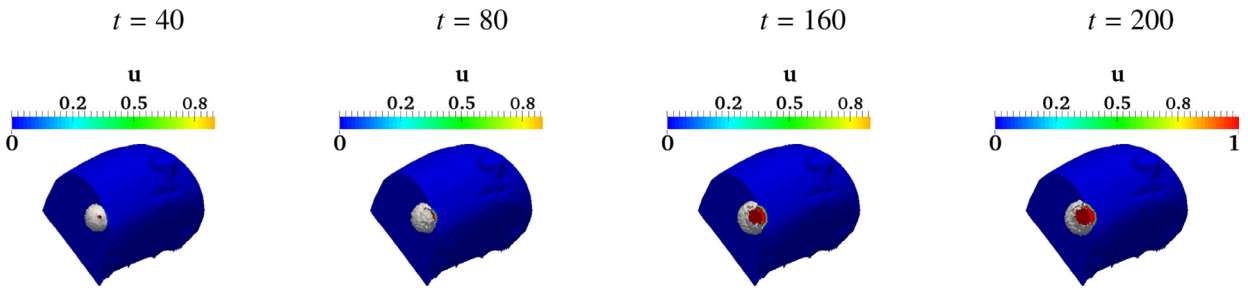

Fig. 14. Sequence of images show the cancer density obtained with the test case (d) at different dimensionless time instances $t = 40,\ 80,\ 160,\ 200$ for different values of model parameters as chosen in the Section 5.1.

We next replace the haptotactic parameter χ as 0.05 and decreased the proliferation rate of cancer cells λ to 0.01 in the same test case (a) to understand the cancer invasion process clearly in realistic domain. Further, all other parameters are remain unchanged. Fig. 11(i) shows the importance of the tumour-matrix components interaction and the haptotaxis effect even with low proliferation rate of the cancer cells. We can observe that a low proliferation rate of cancer cells affects only the speed of the invasion but not the invasion process towards the ECM domain. The simulations confirm that invasion process of the cancer cells would be active with the strong haptotactic sensitivity towards the haptoattractant ECM domain even with low density of cancer cells, see Fig. 11.

Next, we perform simulations with test cases (b) and (c) and the corresponding numerical results are depicted in Figs. 12–14. We observe that the pattern morphology of the cancer density is irregular in shape from the initial spherical form in all three cases. Even though the proliferation and haptotactic rate of the cancer density are same as in the first test case (a), cancer cell migration towards the ECM domain and the corresponding degradation of ECM by producing MDE are not identical in all three cases $(b) - (d)$ in comparison to the case (a) (see Figs. 10 and 12–14). Further, the snapshots of the computations, (Fig. 12–14) assert that the invasion speed of the cancer density is not as fast as in the case of constant diffusion and constant haptotactic function at time $t = 40$ to $t = 200$.

6. Summary

A finite element scheme for computations of three-dimensional cancer invasion mathematical model in realistic geometries is presented. The interactions of cancer cell density with the ECM density and the degradation of the ECM by producing MDE concentration are modeled. Moreover, a nonlinear density-dependent diffusion and haptotactic sensitive functions are

incorporated into the model. In addition to the convergence study and the grid independence test, the proposed scheme is validated using an existing numerical results presented in the literature.

A sequence of computations are performed in order to understand the spatio-temporal behaviors of the cancer invasion process for different nonlinear density-dependent diffusion and haptotactic sensitive functions. Suppose the diffusion function is directly proportional to the MDE concentration we have observed that the migration cancer cells towards the ECM domain is not identical with the constant diffusion rate. However, the cancer cell migration in all other nonlinear diffusion cases is comparable with the constant diffusion. Similarly tumour invasion pattern morphologies formed by Michaelis-Menten kinetics and cooperative binding haptotactic functions are highly distinguishable with other haptotaxis models.

Furthermore, an array of computations of cancer invasion in realistic breast geometry are performed. Grid independence test for the considered realistic geometry is performed with various mesh levels using millions of tetrahedral cells. To get an insight into the cancer invasion on realistic geometries, computational results are presented for different combinations of density-dependent diffusion and haptotactic sensitive functions. Since the boundary effects influence the cancer invasion significantly, it is important to consider a realistic geometry in practical applications.

Finally, the proposed computational model can be used to predict the location and the shape of the tumor in realistic geometries at a particular instance during the cancer growth and invasion. Consequently, the computational model can be extended for cancer treatment monitoring and surgical plannings.

Acknowledgement

The authors would like to thank the anonymous referee for the comments and suggestions which improved the quality of this article. The second author is thankful to the National Board of Higher Mathematics, Department of Atomic Energy (DAE), Mumbai, India for awarding postdoctoral fellowship (Grant No. NBHM/PDF.71/2013/1148) during his stay at Indian Institute of Science, Bangalore.

References

[1] American Cancer Society. Cancer facts & figures. Atlanta: American Cancer Society; 2012. p. 2012.
[2] Anderson ARA, Chaplain MAJ, Newman EL, Steele RJC, Thompson AM. Mathematical modelling of tumor invasion and metastasis. J Theor Med 2000;2:129–54.
[3] Anderson ARA, Chaplain MAJ. Continuous and discrete mathematical models of tumor-induced angiogenesis. Bull Math Biol 1998;60:857–99.
[4] Araujo RP, Mcelwain DLS. A history of the study of solid tumour growth:the contribution of mathematical modelling. Bull Math Biol 2004;66:1039–91.
[5] Bajpai A, Baker JB. Cryptic urokinase binding sites on human foreskin fibroblasts. Biochem Biophys Res Commun 1985;133:475–82.
[6] Bray D. Cell movements: from molecules to motility. Garland Publishing; 2000.
[7] Chaplain MAJ. The mathematical modelling of tumour angiogenesis and invasion. Acta biotheor 1995;43:387–402.
[8] Carpenter CM, Srinivasan S, Pogue BW, Paulsen KD. Methodology development for three-dimensional MR-guided near infrared spectroscopy of breast tumors. Opt Express 2008;16:17903–14.
[9] Chaplain MAJ, Lolas G. Mathematical modelling of cancer cell invasion of tissue: dynamics heterogeneity. Netw Heterog Media 2006;1:399–439.
[10] Chaplain MAJ, Lolas G. Mathematical modelling of cancer cell invasion of tissue: the role of the urokinase plasminogen activation system. Math Models Methods Appl Sci 2005;15:1685–734.
[11] Clatz O, Sermesant M, Bondiau PY, Delingette H, Warfield SK, Malandain G, et al. Realistic simulation of the 3d growth of brain tumors in MR images coupling diffusion with biomechanical deformation. IEEE Trans Med Imaging 2005;24:1334–46.
[12] Daarud AH, van der Zee KG, Oden J. Numerical simulation of a thermodynamically consistent four-species tumor growth model. Int J Numer Meth Biomed Eng 2012;28:3–24.
[13] Davis TA. Algorithm 832: UMFPACK v4.3-an unsymmetric-pattern multifrontal method. ACM Trans Math Softw 2004;30:196–9.
[14] Davis TA. A column pre-ordering strategy for the unsymmetric-pattern multifrontal method. ACM Trans Math Softw 2004;30:167–95.
[15] Epshteyn Y. Discontinuous galerkin methods for the chemotaxis and haptotaxis models. J Comput Appl Math 2009;224:168–81.
[16] Enderling H, Chaplain MAJ. Mathematical modeling of tumor growth and treatment. Curr Pharm Des 2014;20:4934–40.
[17] Enderling H, Anderson ARA, Chaplain MAJ, Munro AJ, Vaidya JS. Mathematical modelling of radiotherapy strategies for early breast cancer. J Theor Biol 2006;241:158–71.
[18] Ganesan S, Tobiska L. An accurate finite element scheme with moving meshes for computing 3d-axisymmetric interface flows. Int J Numer Meth Fluids 2008;57:119–38.
[19] Gerisch A, Chaplain MAJ. Mathematical modelling of cancer cell invasion of tissue:local and non-local models and the effect of adhesion. J Theor Biol 2008;250:684–704.
[20] Gavaghan DJ, Brady JM, Behrenbruch CP, Highnam RP, Maini PK. Breast cancer: modelling and detection. J Theor Med 2002;4:3–20.
[21] Hillen T, Painter KJ. A users guide to PDE models for chemotaxis. J Math Biol 2009;58:183–217.
[22] Jemal A, Tiwari RC, Murray T, Ghafoor A, Samueis A, Ward E, et al. Cancer statistics. CA Cancer J Clin 2004;54:9–29.
[23] Jin H.Y., Xiang T.. Boundedness and exponential convergence of a chemotaxis model for tumor invasion. 2016. ArXiv:1604.03898.
[24] Kolbe N., Katuchova J., Sfakianakis N., Hellmann N., Lukacova-Medvidova M.. Numerical study of cancer cell invasion dynamics using adaptive mesh refinement: the urokinase model. ArXiv:1408.0942v1.
[25] Kowalczyk R. Preventing blow-up in a chemotaxis model. J Math Anal Appl 2005;305:566–88.
[26] Lowengrub JS, Frieboes HB, Jin F, Chuang YL, Li X, Macklin P, et al. Nonlinear modelling of cancer: bridging the gap between cells and tumours. Nonlinearity 2010;23:R1–R91.
[27] Meral G, Surulesu C. Mathematical modelling, analysis and numerical simulations for the influence of heat shock proteins on tumour invasion. J Math Anal Appl 2014;408:597–614.
[28] Nava G, Greer K, Patterson J, Lin KY. Metastatic cutaneous breast carcinoma: a case report and review of the literature. Can J Plast Surg 2009;17:25–7.
[29] Orme ME, Chaplain MAJ. A mathematical model of vascular tumour growth and invasion. Math Comput Modell 1996;23:43–60.
[30] Papadogiorgaki1 M, Koliou P, Kotsiakis X, Zervakis ME. Mathematical modelling of spatio-temporal glioma evolution. Theor Biol Med Model 2013;10:1–32.
[31] Peterson JW, Carey GF, Knezevic DJ, Murray BT. Adaptive finite element methodology for tumour angiogenesis modelling. Int J Numer Meth Biomed Engng 2007;69:1212–38.
[32] Roose T, Chapman SJ, Maini PK. Mathematical models of avascular tumor growth. SIAM Rev 2007;49:179–208.
[33] Sherratt JA, Murray JD. Models of epidermal wound healing. Proc R Soc B 1990;241:29–36.

[34] Sherratt JA. Chemotaxis and chemokinesis in eukaryotic cells: the keller-segel equations as an approximation to a detailed model. Bull Math Biol 1994;56:129–46.
[35] Sokolov A, Ali R, Turek S. An AFC-stabilized implicit finite element method for partial differential equations on evolving-in-time surfaces. J Comput Appl Math 2015;289:101–15.
[36] Stepien TL, Rutter EM, Kuang Y. A data-validated density-dependent diffusion model of glioblastoma growth. Math Biosc Eng 2015;12:1157–72.
[37] Strehl R, Sokolov A, Kuzmin D, Horstmann D, Turek S. A positivity-preserving finite element method for chemotaxis problems in 3d. J Comput Appl Math 2013;239:290–303.
[38] Strehl R, Sokolov A, Kuzmin D, Horstmann D, Turek S. Efficient, accurate and flexible finite element solvers for chemotaxis problems. Comput Math Appl 2012;64:175–89.
[39] Stokes CL, Lauffenburger DA, Williams SK. Migration of individual microvessel endothelial cells: stochastic model and parameter measurement. J Cell Sci 1991;99:419–30.
[40] Tao Y, Winkler M. Large time behavior in a multidimensional chemotaxis-haptotaxis model with slow signal diffusion. SIAM J Math Anal 2015;47:4229–50.
[41] Tao Y, Cui C. A density-dependent chemotaxis-haptotaxis system modeling cancer invasion. J Math Anal Appl 2010;367:612–24.
[42] Tracqui P. Biophysical models of tumor growth. Rep Prog Phys 2009;72:056701.
[43] Vilanova G, Colominas I, Gomez H. Capillary networks in tumor angiogenesis: from discrete endothelial cells to phase-field averaged descriptions via isogeometric analysis. Int J Numer Meth Biomed Eng 2013;29:1015–37.
[44] Yu W, Kim J, Ossowski L. Reduction in surface urokinase receptor forces malignant cells into a protracted state of dormancy. J Cell Biol 1997;137:767–77.
[45] Zheng X, Wise SM, Cristini V. Nonlinear simulation of tumor necrosis, neovascularization and tissue invasion via an adaptive finite-element/level set method. Bull Math Biol 2005;67:211–59.